

CsCu₂I₃ Nanoparticles Incorporated within a Mesoporous Metal–Organic Porphyrin Framework as a Catalyst for One-Pot Click Cycloaddition and Oxidation/Knoevenagel Tandem Reaction

Saba Daliran, Mostafa Khajeh,* Ali Reza Oveisi,* Josep Albero, and Hermenegildo García*



Cite This: *ACS Appl. Mater. Interfaces* 2022, 14, 36515–36526



Read Online

ACCESS |

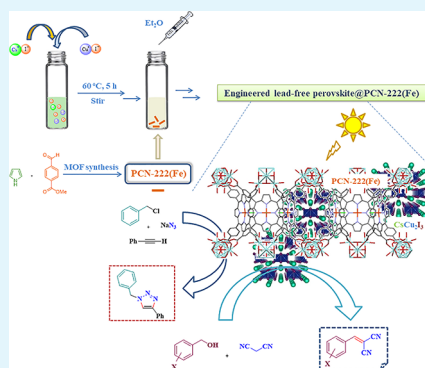
Metrics & More

Article Recommendations

Supporting Information

ABSTRACT: Metal–organic frameworks (MOFs) and metal halide perovskites are currently under much investigation due to their unique properties and applications. Herein, an innovative strategy has been developed combining an iron-porphyrin MOF, PCN-222(Fe), and an *in situ*-grown CsCu₂I₃ nontoxic lead-free halide perovskite based on an earth-abundant metal that becomes incorporated within the MOF channels [CsCu₂I₃@PCN-222(Fe)]. Encapsulation was designed to decrease and control the particle size and increase the stability of CsCu₂I₃. The hybrid materials were characterized by various techniques including FE-SEM, elemental mapping and line scanning EDX, TEM, PXRD, UV–Vis DRS, BET surface area, XPS, and photoemission measurements. Hybrid CsCu₂I₃@PCN-222(Fe) materials were examined as heterogeneous multifunctional (photo)catalysts for copper(I)-catalyzed alkyne-azide cycloaddition (CuAAC) and one-pot selective photo-oxidation/Knoevenagel condensation cascade reaction. Interestingly, CsCu₂I₃@PCN-222(Fe) outperforms not only its individual components CsCu₂I₃ and PCN-222(Fe) but also other reported (photo)-catalysts for these transformations. This is attributed to cooperation and synergistic effects of the PCN-222(Fe) host and CsCu₂I₃ nanocrystals. To understand the catalytic and photocatalytic mechanisms, control and inhibition experiments, electron paramagnetic resonance (EPR) measurements, and time-resolved phosphorescence were performed, revealing the main role of active species of Cu(I) in the click reaction and the superoxide ion (O₂^{•-}) and singlet oxygen (¹O₂) in the photocatalytic reaction.

KEYWORDS: heterogeneous catalysis, metal–organic frameworks as hosts, CsCu₂I₃ perovskite, multifunctional catalyst, photo-oxidation



1. INTRODUCTION

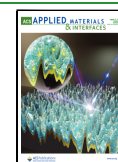
Perovskites, as semiconductors, are prospective materials for emerging optoelectronic applications owing to their remarkable physical and chemical features, low manufacturing cost, and adjustable tenability.^{1,2} Lead-based perovskites, as the most common perovskites, can be highly efficient for light harvesting; however, they exhibit very low stability and high toxicity, which limit their practical applications.^{3,4} Therefore, intensive research has been conducted to develop alternative low toxicity and efficient lead-free perovskites. Among the newly studied lead-free candidates, copper-based perovskites are among the most promising. Particularly, 1D CsCu₂I₃ exhibits a decent photoresponse and lesser toxicity as well as being constituted by the earth-abundant Cu element.^{1,5–8} However, there are some critical points that hamper Cu perovskite preparation, such as the need to add multiple capping agents to limit crystal growth and to stabilize the structure, the use of DMF as a solvent, and/or long crystal growth time. Furthermore, due to their lack of structural stability, the activity of Cu perovskites in (photo)catalysis is largely unexplored, which is important to gain information of their properties as catalysts.

Typically, instable perovskites, such as lead halide perovskites, are stabilized on silica/alumina^{9,10} or polymer supports,¹¹ but frequently, the perovskite is not homogeneously distributed, there are substrate diffusion limitations, and there is metal leaching to the liquid phase. One alternative strategy is to use periodic, well-defined metal–organic frameworks (MOFs) as supports.^{12–15} Metal–organic frameworks (MOFs), formed by inorganic nodes and organic connectors interacting by Coulombic and coordination bonds, are highly crystalline and well-defined unique porous frameworks with variable structures and chemical functionalities, tunable pore sizes, high specific surface areas, large internal pore volumes, and low framework densities.^{16,17} Because of these intrinsic features, MOFs have been massively studied in various areas.^{17–22}

Received: March 28, 2022

Accepted: July 26, 2022

Published: August 8, 2022



Research has shown that hybridization of perovskites with MOFs results in the formation of new multicomponent materials with enhanced stability, higher efficiency, and improved charge transfer and performance compared to the individual components^{12–15} or classical supports.^{9–11} However, most of reported MOF supports possess micropores (<2 nm), which restricted the mass diffusion and perovskite growth and affected the stability of the MOF structure.^{14,15} Therefore, to address these issues, MOFs with ordered mesopores and high porosity, maintaining their stability during and after perovskite loading, are highly demanded but challenging. Particularly, the stabilization of 0D or 1D perovskites provided by encapsulation within MOFs can enable evaluation of the catalytic activity of occluded halide perovskites, something that has remained elusive so far. In addition, the MOF can cooperate with the activity of the occluded perovskite, producing a synergy between the two components in a multifunctional material.

PCN-222(Fe) is a distinctive metalloporphyrin MOF with a high surface area involving Zr₆ clusters attached to Fe-TCPP (TCPP = 4,4',4'',4'''-(porphine-5,10,15,20-tetrayl)tetrakis-(benzoic acid)) linkers. In addition, PCN-222(Fe) possesses regular hexagonal meso- and triangular microporous channels and high thermal and chemical stability,^{23–26} inside which CsCu₂I₃ can be accommodated.

Herein, it is shown that encapsulation of the CsCu₂I₃ perovskite inside a mesoporous iron-porphyrin PCN-222(Fe) MOF as a host can be achieved by a facile *in situ* growth to render CsCu₂I₃@PCN-222(Fe). By varying the synthetic parameters, CsCu₂I₃ units uniformly distributed in PCN-222(Fe) and having a strong interaction with the PCN-222(Fe) framework can be prepared. PCN-222(Fe) functions as a support, stabilizing and confining the size and shape of the encapsulated CsCu₂I₃ nanostructures. Stabilization provided by PCN-222(Fe) has allowed the study of the activity of CsCu₂I₃ as a heterogeneous catalyst for a three-component CuAAC reaction and one-pot cascade photo-oxidation of benzyl alcohols/Knoevenagel coupling reaction. It was observed that CsCu₂I₃@PCN-222(Fe) exhibits high activity for these reactions, outperforming the individual components and other reported catalysts. Remarkably, CsCu₂I₃@PCN-222(Fe) was stable and could be easily recovered from the reaction media for reuse with no obvious decay in activity. This stability is remarkable considering the notorious instability characteristic of halide perovskites. Mechanistic studies indicated a synergistic cooperation between CsCu₂I₃ and PCN-222(Fe). In addition, the host–guest system was further confirmed by using various techniques as described here. The design of multifunctional solid catalysts based on nontoxic elements and the characterization of the synergistic effects derived from the encapsulation of CsCu₂I₃, well studied in the field of photovoltaics but not in catalysis, are two of the current research fronts in advanced materials synthesis.

2. EXPERIMENTAL SECTION

2.1. Materials. Chemical materials such as pyrrole, methyl benzaldehyde-4-carboxylate, propionic acid, benzoic acid, zirconium(IV) chloride, iron dichloride tetrahydrate, *N,N'*-diethylformamide (DEF), cesium iodide, copper(I) iodide, acetonitrile, sodium azide, benzyl chloride, phenylacetylene, malononitrile, and benzyl alcohols were synthetically pure and were supplied by Merck. The Fe-TCPP linker was synthesized following a procedure described in the literature.²³ PCN-222(Fe) was synthesized and activated with the HCl-treatment procedure.²³ Synthesis of pure CsCu₂I₃ perovskite was

performed by a modified procedure reported in the literature⁷ as mentioned here.

2.2. Characterization. High-quality X-ray diffraction patterns were acquired with Cu K_{α1} radiation on a Philips, X'Pert XRD diffractometer (Netherlands). FE-SEM imaging, energy dispersive X-ray spectroscopy (EDX), and elemental mapping measurements were performed on a scanning electron microscope (TESCAN MIRA3, Czech Republic). Thermogravimetric analysis (TGA) tests were conducted on a TGA/DSC instrument (Mettler Toledo, Germany) under an inert atmosphere. Nitrogen adsorption/desorption isotherms at −196 °C were obtained on an ASAP apparatus (Micromeritics, USA). The NMR spectra of the products were recorded on a Bruker Avance DPX-250 NMR (300 MHz for ¹H NMR and 75 MHz for ¹³C NMR) in deuterated solvents. The diffuse reflectance spectra were collected by using ultraviolet–visible diffuse reflectance spectroscopy (UV–Vis DRS, Shimadzu Co., Japan). The visible exposure was achieved by 280 power light-emitting diode (LED) lamps (3.2 V, 1 W) in a cylindrical container, 32,000 LUX, including air cooling fans to keep the temperature constant at 31–35 °C. The X-ray photoelectron spectra (XPS) were measured on a SPECS spectrometer equipped with a Phoibos 150 9MCD detector using a nonmonochromatic X-ray source (Al) operating at 200 W. The samples were evacuated in the prechamber of the spectrometer at 1 × 10^{−9} mbar. The measured intensity ratios of the components were obtained from the area of the corresponding peaks after nonlinear Shirley-type background subtraction and corrected by the transition function of the spectrometer. The work function of the apparatus was calibrated with Ag, Au, and Cu with a value of 4.2440 eV. The EPR spectra were recorded using a Bruker EMX, with the typical settings: frequency, 9; 80 GHz; sweep width, 100 G; time constant, 80 ms; modulation frequency, 100 kHz; modulation width, 0.2 G. Singlet oxygen was studied by time-resolved near-infrared phosphorescence using a home-made setup. Briefly, a pulsed Nd:YAG laser (FTSS355-Q, Crystal Laser) working at 1 kHz repetition rate at 355 nm (third harmonic; 0.5 μJ per pulse) was used for sample excitation. A 1064 nm Rugate notch filter (Edmund Optics) and an uncoated SKG-5 filter (CVI Laser Corporation) were placed at the exit port of the laser to remove any residual component of its fundamental emission in the near-infrared region. The luminescence exiting from the sample was filtered by a 1100 nm long-pass filter (Edmund Optics) and a narrow bandpass filter at 1275 nm (BK-1270-70-B, bk Interferenzoptik). A thermoelectric-cooled near-infrared sensitive photomultiplier tube assembly (H9170-45, Hamamatsu Photonics) was used as a detector. High-resolution TEM (HRTEM) images, scanning TEM (STEM) images, and energy-dispersive X-ray (EDX) spectra were recorded by using a JEOL, JEM 2100F microscope. Steady-state fluorescence measurements were carried out using a Photon Technology International (PTI, Germany) LPS-220B spectrofluorometer equipped with a monochromator in the range of 200–800 nm. The excitation wavelength was 360 nm and emission was recorded from 390 to 700 nm by 1 nm steps with an integration time of 0.1 s, averaging three measurements.

2.3. Synthesis of CsCu₂I₃. CuI (1.3 mmol) and CsI (0.65 mmol) were added to a glass vial containing anhydrous acetonitrile (4 mL) before stirring at 60 °C for 5 h. Then, the vial was allowed to cool to room temperature and the saturated solution was filtered through a polytetrafluoroethylene (PTFE) (0.45 μm) filter adapted to a syringe. After that, diethyl ether (~2 mL) was added dropwise to the filtered solution. The white precipitate of CsCu₂I₃ formed was allowed to grow for 15 min or 3.5 h and collected by centrifugation.

2.4. CsCu₂I₃ Confined into PCN-222(Fe). CsCu₂I₃@PCN-222(Fe) nanostructures were fabricated by controlling the reaction time and temperature using the so-called antisolvent/inverse solvent infiltration approach. Briefly, CuI (1.3 mmol) and CsI (0.65 mmol) were sonicated in acetonitrile (4 mL) and stirred magnetically for 5 h at 60 °C. The mixture was cooled to ambient temperature, filtered through a polytetrafluoroethylene (PTFE) (0.45 μm) syringe, and further injected into glass vials containing activated PCN-222(Fe) (50 mg) before being capped and kept in ambient temperature or 60 °C for 16–18 h. After refreshing the top of the solvent, the CsCu₂I₃

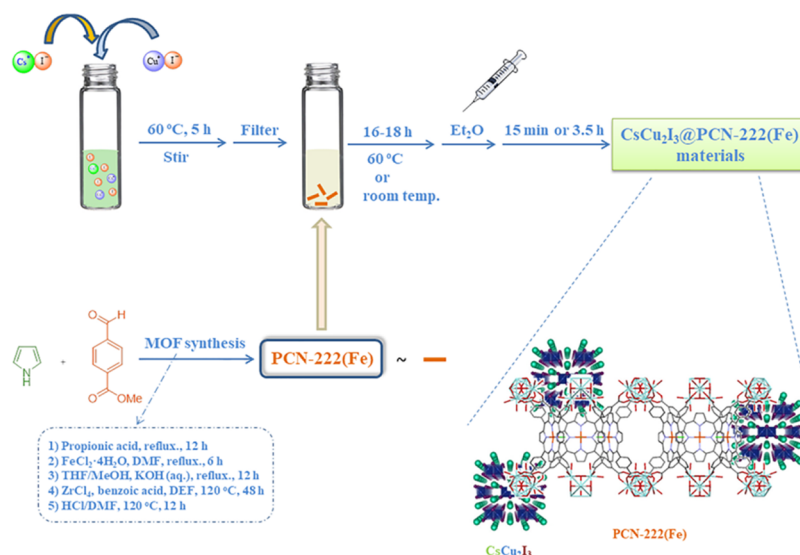


Figure 1. Synthesis route used for the preparation of $\text{CsCu}_2\text{I}_3@\text{PCN-222(Fe)}$ hybrid materials.

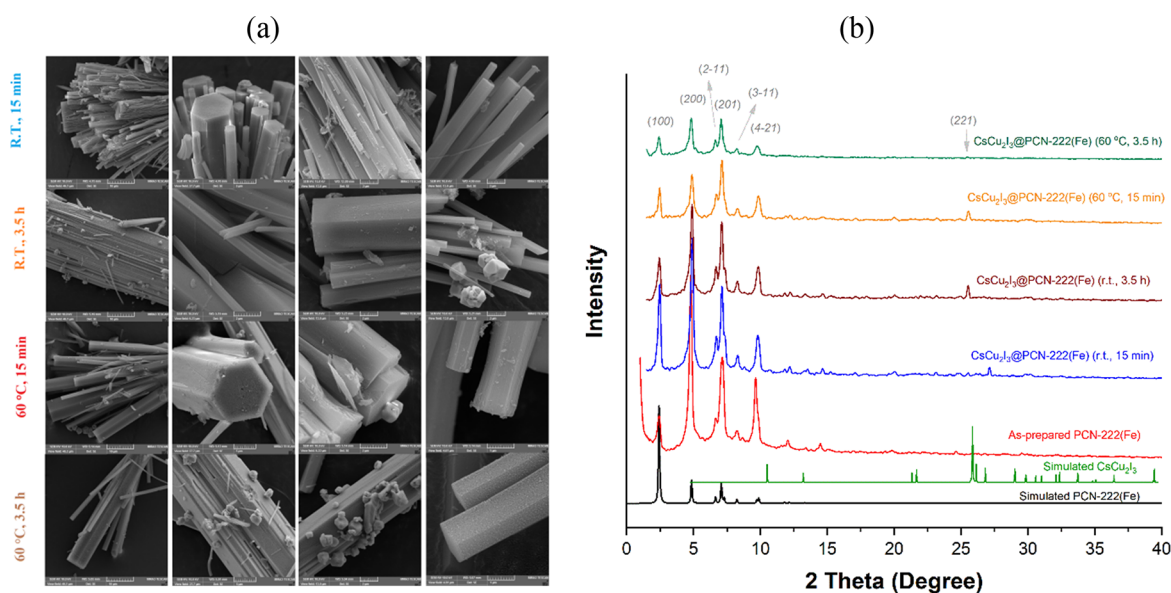


Figure 2. (a) SEM images at four different magnifications (from left to right: 10, 5, 2, and 1 μm) of as-synthesized $\text{CsCu}_2\text{I}_3@\text{PCN-222(Fe)}$ hybrid materials under the different conditions (15 min-r.t., 3.5 h-r.t., 15 min-60 $^{\circ}\text{C}$, and 3.5 h-60 $^{\circ}\text{C}$) and (b) XRD patterns of simulated MOF, simulated CsCu_2I_3 , and as-prepared MOF and $\text{CsCu}_2\text{I}_3@\text{MOF}$ hybrid materials obtained at different times and temperatures (15 min-r.t., 3.5 h-r.t., 15 min-60 $^{\circ}\text{C}$, and 3.5 h-60 $^{\circ}\text{C}$).

crystals were allowed to grow at room temperature by dropwise addition of diethyl ether as an antisolvent (~ 2 mL). As-synthesized $\text{CsCu}_2\text{I}_3@\text{PCN-222(Fe)}$ materials with different amounts of CsCu_2I_3 were then washed several times with acetonitrile and acetone to give $\text{CsCu}_2\text{I}_3@\text{PCN-222(Fe)}$ hybrid materials, here namely, 15 min-r.t., 3.5 h-r.t., 15 min-60 $^{\circ}\text{C}$, and 3.5 h-60 $^{\circ}\text{C}$.

2.5. One-Pot Three-Component Click Reaction. In an unsealed vial, benzyl chloride (0.5 mmol), sodium azide (1 mmol), and phenyl acetylene (1 mmol) were mixed in H_2O (2 mL) and then the catalyst (10 mg) was added. The resulting mixture was stirred at room temperature and periodically checked by TLC (*n*-hexane/ethyl acetate (4:1)). After the completion of the reaction, the mixture was diluted by additional H_2O (4 mL), and the catalyst was removed by centrifugation and washed with ethyl acetate. The organic layer was extracted three times with ethyl acetate, washed with saturated NaHCO_3 , and passed over anhydrous Na_2SO_4 . Recrystallization from a mixture of ethyl acetate and hexane afforded the pure product.

2.6. Tandem Photo-oxidation/Knoevenagel Condensation Reaction. Into a test tube, benzyl alcohol (0.5 mmol), malononitrile (0.75 mmol), acetonitrile (2–3 mL), and catalyst (15 mg) were mixed and then the mixture was stirred at room temperature under exposure to visible LED illumination and oxygen (an O_2 -filled balloon). The temperature in the illuminated photoreactor was maintained at 33 ± 2 $^{\circ}\text{C}$. After completion of the reaction, the mixture was checked by TLC (*n*-hexane/ethyl acetate (5:1)), the catalyst was extracted by centrifugation, and the solvent was evaporated under vacuum. The product was finally purified by recrystallization from ethanol/water.

3. RESULTS AND DISCUSSION

3.1. Synthesis and Characterization of $\text{CsCu}_2\text{I}_3@\text{PCN-222(Fe)}$. $\text{CsCu}_2\text{I}_3@\text{PCN-222(Fe)}$ samples with different porosity, sizes, pore structures, surface areas, and morphology were fabricated by controlling the reaction time and temper-

ature employing an antisolvent/inverse solvent infiltration approach using the MOF support (after its synthesis) and CsCu_2I_3 precursors as shown in Figure 1 (see Section 2 for details). The use of an Fe-porphyrin avoids subsequent partial metalation of free-base porphyrin during the synthesis of halide perovskite while shortening the bandgap of PCN-222 and ensuring a strong O_2 adsorption.

Field emission scanning electron microscopy (FE-SEM) images of as-synthesized $\text{CsCu}_2\text{I}_3@$ PCN-222(Fe) (15 min-r.t., 3.5 h-r.t., 15 min-60 °C, and 3.5 h-60 °C, denoting the time and temperature of the PCN-222 infiltration treatment), individual CsCu_2I_3 , and pristine PCN-222(Fe) are shown in Figure 2a and Figure S1.

At a short time (15 min), the images clearly display the selective growth of CsCu_2I_3 with rod-like morphology along the c axis of hexagonal rod-shaped PCN-222(Fe) crystals. In addition, when the antisolvent was added and aged for 3.5 h, CsCu_2I_3 nanocrystals were further grown with irregular octahedron-like morphology especially apparent on the surface. It was obvious that the presence of the MOF takes control the growth rate and crystal size of CsCu_2I_3 , effectively avoiding the agglomeration of the growing crystals (see Figure S1 versus Figure 2a). As shown in the SEM images of Figure 2a and Figure S1, under otherwise identical conditions, smaller CsCu_2I_3 crystals are obtained in the presence of PCN-222(Fe) owing to its well-defined ordered porous structure, while bigger and enlarged CsCu_2I_3 crystals or large agglomerations are fabricated in the absence of the MOF. Furthermore, the results showed that the reaction time had more significant influence on the CsCu_2I_3 particle size and morphology than the reaction temperature.

Elemental composition of the synthesized samples determined by energy-dispersive X-ray spectroscopy (EDX) confirmed the presence of all the expected elements, namely, C, N, O, Fe, Cu, Zr, I, and Cs, showing the relative Cu/Cs molar ratios of 1.73, 1.99, 2.33, and 1.91, respectively, for the 15 min-r.t., 3.5 h-r.t., 15 min-60 °C, and 3.5 h-60 °C $\text{CsCu}_2\text{I}_3@$ PCN-222(Fe) samples (Table S1), in fair agreement with the expected values. Furthermore, EDX elemental mapping of the structures indicated the uniform distribution of all the constituents (C, N, O, Fe, Cu, Zr, I, and Cs) over the $\text{CsCu}_2\text{I}_3@$ PCN-222(Fe) crystals (Table S2).

The crystalline structures and successful synthesis of the $\text{CsCu}_2\text{I}_3@$ PCN-222(Fe) hybrid materials were further proven by X-ray diffraction (XRD) patterns (Figure 2b), which evidently exhibited the diffraction peaks of PCN-222(Fe), whose main peaks at 2θ of 2.5°, 4.8°, 6.6°, 7.1°, 8.2°, and 9.8° correspond to diffraction through the (100), (200), (2-11), (201), (3-13), and (4-21) planes (CCDC no. 893545), respectively,²³ and CsCu_2I_3 , whose main diffraction peak at 2θ of 26.1° corresponds to diffraction in the (221) plane (PDF #45-0076). The PXRD patterns indicated that the growth of CsCu_2I_3 crystals had no effect on the PCN-222(Fe) structure. The experimental PXRD data of as-synthesized CsCu_2I_3 particles match well with the standard pattern of CsCu_2I_3 (Figure S2).^{27,28} The peaks at $2\theta = 10.8^\circ, 13.5^\circ, 21.6^\circ, 21.9^\circ, 26.1^\circ, 27.2^\circ, 29.3^\circ, 33.6^\circ, 32.6^\circ,$ and 39.8° can be ascribed respectively to the reflections from the (110), (020), (220), (130), (221), (040), (002), (202), (330), and (421) crystal planes of the orthorhombic phase. No difference in the XRD pattern of CsCu_2I_3 for the rod- or octahedron-like particles was observed.

To investigate the permanent porosity of the samples, isothermal N_2 adsorption–desorption measurements at 77 K were performed (Figure 3 and Figure S3). The N_2 isotherms

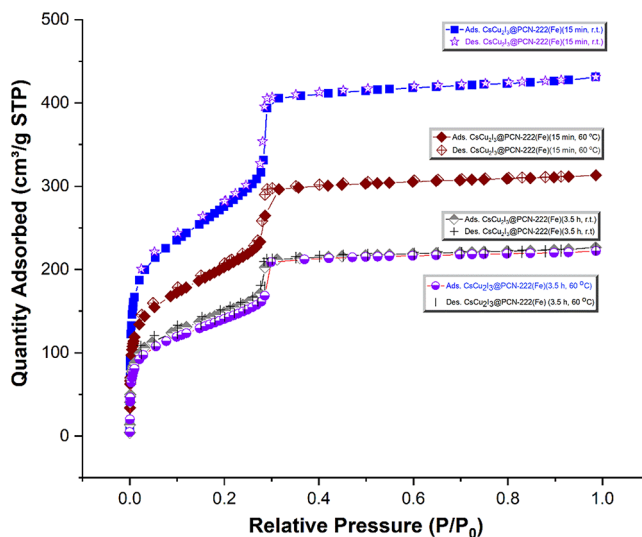


Figure 3. N_2 adsorption–desorption isotherms for $\text{CsCu}_2\text{I}_3@$ PCN-222(Fe) hybrid materials at 77 K (from top to bottom: 15 min-r.t., 15 min-60 °C, 3.5 h-r.t., and 3.5 h-60 °C).

show a distinctive IUPAC type IV shape, revealing the existence of mesopores (a steep rise at about $P/P_0 = 0.3$) for all of them. The measured Brunauer–Emmett–Teller (BET) surface areas for PCN-222(Fe) and $\text{CsCu}_2\text{I}_3@$ PCN-222(Fe) samples of 15 min-r.t., 3.5 h-r.t., 15 min-60 °C, and 3.5 h-60 °C were calculated to be 1715, 930, 500, 682, and 480 $\text{m}^2 \text{g}^{-1}$, respectively (Figure 3 and Figure S3). The observed decreases in BET surface areas are attributed to the *in situ* growth of CsCu_2I_3 into the PCN-222(Fe) MOF voids at different loadings and the pore-filling effect, in good agreement with the information provided by SEM/EDX data.

The porosity of PCN-222(Fe) and $\text{CsCu}_2\text{I}_3@$ PCN-222(Fe) structures with tunable pores was further confirmed by using nonlocal density functional theory models to determine pore size distributions (PSDs). As a result, the pore diameters of PCN-222(Fe) after the *in situ* growth and immobilization of the CsCu_2I_3 perovskite decreased as the reaction time and temperature increased, proving further the successful synthetic steps (see Figures S3 and S4 in detail).

The UV–Vis DRS spectra of $\text{CsCu}_2\text{I}_3@$ PCN-222(Fe) samples containing different amounts of CsCu_2I_3 perovskite recorded at room temperature are shown in Figure S5. Comparison of the UV–Vis DRS spectra of $\text{CsCu}_2\text{I}_3@$ PCN-222(Fe) with those of PCN-222(Fe) shows, as the most remarkable feature, the appearance of an intense peak around 200–400 nm, which can be attributed to the CsCu_2I_3 perovskite, and notably, the absorbance of $\text{CsCu}_2\text{I}_3@$ PCN-222(Fe) samples covered the entire UV–Vis area. In addition, these UV–Vis DRS spectra indicate that there is a strong interaction between PCN-222(Fe) and the CsCu_2I_3 guest, leading to changes in the measured spectra of the hybrid material with respect to the sum of the two components. The observed differences in the UV–Vis DRS spectra of the host–guest hybrids might be because of the different loadings of the CsCu_2I_3 perovskite. Furthermore, the optical bandgaps (E_g) were estimated from the plot of $(\alpha h\nu)^{1/2}$ versus photon energy

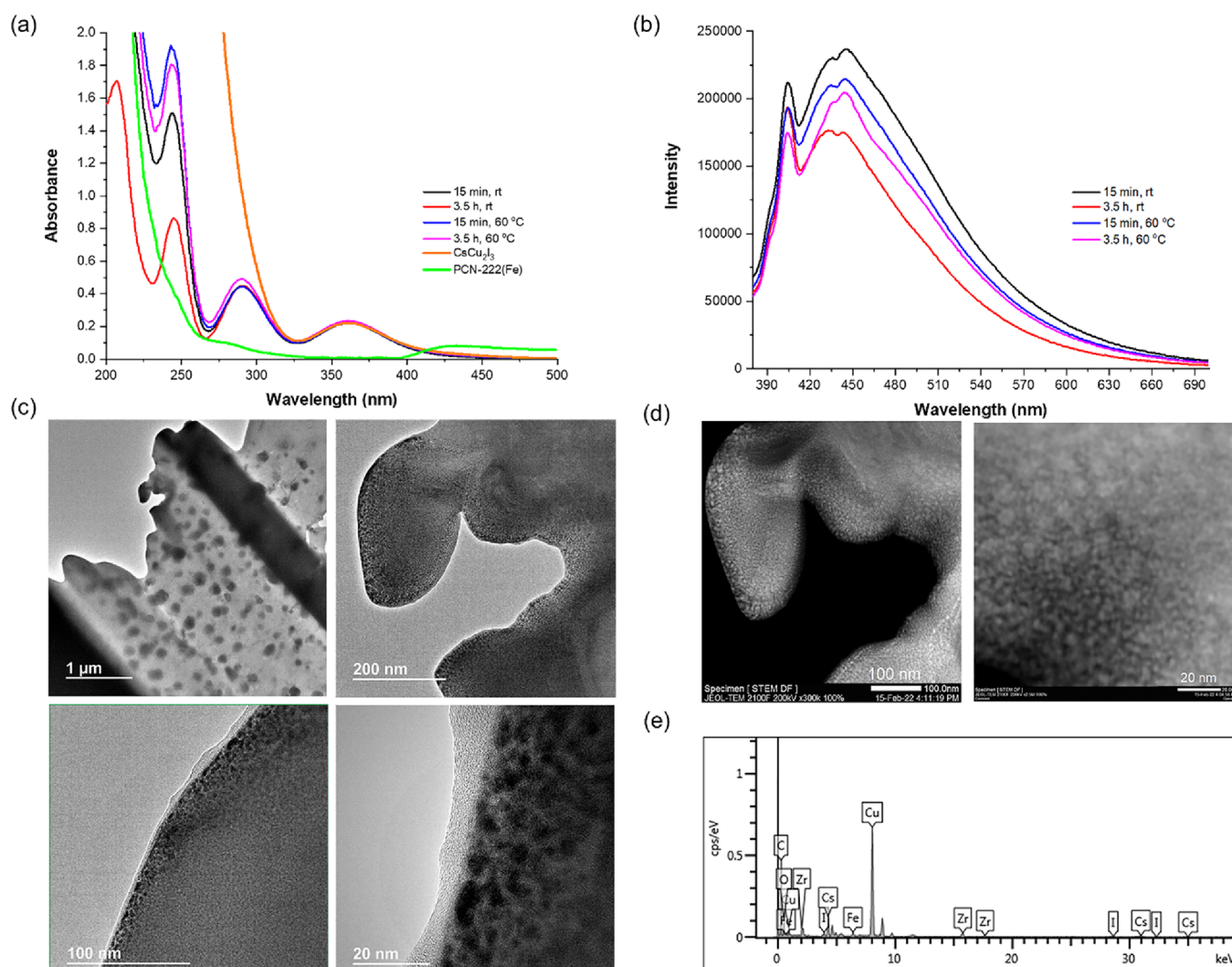


Figure 4. (a) Steady-state UV–Vis extinction, (b) emission spectra of CsCu₂I₃@PCN-222(Fe) composites ($\lambda_{\text{exc}} = 360$ nm), (c) HRTEM images, and (d) STEM images along with (e) EDX analysis.

($h\nu$) (the Tauc equation) obtained from the diffuse reflectance data (Figure S6). As seen in Figure S6, the E_g values of CsCu₂I₃@PCN-222(Fe) samples estimated from the intercept of tangents to the Tauc plots were between ~ 1.54 and 1.59 eV. Notably, these values are lower than that of the CsCu₂I₃ perovskite (~ 3.78 eV).^{1,5,7,8}

The presence of the CsCu₂I₃ perovskite inside PCN-222 is revealed using UV–Vis absorption spectroscopy by the appearance of the characteristic absorption band at 360 nm. Additionally, the composites exhibit different fluorescence spectra than the individual components (Figure 4a,b), indicating that incorporation of CsCu₂I₃ inside the porphyrin MOF establishes an electronic guest (perovskite)–host (PCN-222) interaction that alters the emission properties. Particularly notable is the position of λ_{em} for the maximum emission intensity that appears to be blue-shifted with respect to 1D CsCu₂I₃, which typically appears at $\lambda_{\text{em}} > 500$ nm. The λ_{em} value of about 450 nm corresponds better to nanoparticles of Cu perovskites due to their small particle size (see below).

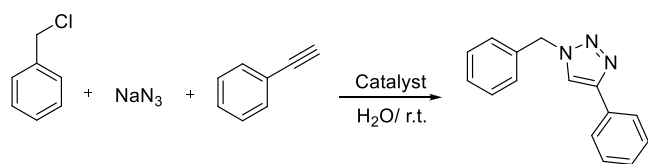
The presence of the CsCu₂I₃ perovskite was also evidenced by X-ray photoelectron spectroscopy (XPS) measurements. Figure S7 displays the XPS spectra of the Cu (2p) region for the whole series of CsCu₂I₃@PCN-222(Fe). All samples

exhibit strong Cu 2p_{1/2} (952.4 eV) and Cu 2p_{3/2} (932.4 eV) peaks without any noteworthy Cu(II) satellites at ~ 942 and ~ 962 eV, demonstrating that the oxidation state corresponds predominantly to Cu(I) in agreement with the formation of the lead-free CsCu₂I₃ perovskite.²⁹ Interestingly, these results also indicate that the mesoporous MOF environment successfully prevents the oxidation of Cu⁺ to Cu²⁺ even after prolonged thermal treatments. To further confirm the synergistic effects of the PCN-222(Fe) host and CsCu₂I₃ nanocrystals, XPS peaks of Cs, Cu, and I in CsCu₂I₃ and CsCu₂I₃@PCN-222(Fe) samples were compared (Figure S8). For CsCu₂I₃, the characteristic peak of Cs 3d can be deconvoluted in two components: Cs⁺ at 737.6 eV and Cs–I at 723.69 eV. The Cu 2p spectrum peak is fitted to a Cu–I bond at 931.20 eV.^{27,30,31} The I 3d characteristic peaks are attributed to two bonds, Cs–I at 618.11 eV and Cu–I at 619.37 eV.^{27,30} It should be noted that the C 1s and O 1s peaks, likely coming from the solvent, are also detected. The notable binding energy shifts are observed in the XP spectra of the composite compared to those of pristine CsCu₂I₃ (see Figure S8 for details). Also, the elemental signals of the CsCu₂I₃@PCN-222(Fe) hybrid show relatively broad peaks as compared to those of CsCu₂I₃.

Images of the CsCuI₃ perovskite inside the MOF crystals could be obtained by cutting thin nanometric slices of the CsCu₂I₃@PCN-222(Fe) material using fast ion bombardment (FIB) and placing these slices in a high-resolution scanning transmission electron microscope. The specimens were thin enough to allow electron transmission imaging. As can be seen in Figure 4c, although large dark dots of about 100 nm corresponding to the CsCuI₃ perovskite were already observed at low magnification, they are most probably due to artifacts formed during the FIB process. At higher magnifications, the STEM images show a very good dispersion of CsCuI₃ dots all around the PCN-222(Fe) matrix (Figure 4d). A considerable number of particles between 2 and 4 nm were clearly visualized in the STEM images, accompanied by larger particles between 5 and 10 nm. It is proposed that the larger particles are formed by agglomeration of the smaller CsCuI₃ particles as a consequence of the FIB manipulation. Dark-field images and EDX analysis confirm that these dots are constituted by Cu, Cs, and I (Figure 4e). Therefore, the HR-STEM study shows a very good dispersion of CsCu₂I₃ with a considerable fraction of CsCuI₃ particles having a size commensurate with PCN-222 channel dimensions of about 3.2 nm, compatible with the internal incorporation of CsCu₂I₃.

3.2. Catalytic Properties of PCN-222(Fe)-Encapsulated CsCu₂I₃. Copper(I)-catalyzed intermolecular alkyne-azide cycloaddition (CuAAC) reaction, also named as the Sharpless “click” reaction, was reported in 2001³² and used for the synthesis of triazoles as fine chemicals³³ and for the efficient covalent surface functionalization and covalent attachment under mild conditions.²¹ Therefore, the catalytic activity of the CsCu₂I₃@PCN-222(Fe) composites was first evaluated for the CuAAC reaction. In this regard, the catalytic performance of the CsCu₂I₃@PCN-222(Fe) hybrids was investigated in a new click reaction version, one-pot three-component type. The results are summarized in Table 1. Remarkably, CsCu₂I₃@PCN-222(Fe) (15 min-r.t., with 0.8 wt % copper and 11.47 wt % zirconium) promoted the reaction at ambient temperature in aqueous media, a naturally abundant and green solvent, and gave the isolated 1,4-diphenyltriazole product with a yield of 98% and a high selectivity of 99.9%

Table 1. One-Pot Three-Component CuAAC Reaction by Different Catalysts^a



entry	catalyst (mg)	time (min)	yield (%) ^b
1	CsCu ₂ I ₃ @PCN-222(Fe)-15 min-r.t. (10)	85	98
2	CsCu ₂ I ₃ @PCN-222(Fe)-15 min-60 °C (10)	80	98
3	CsCu ₂ I ₃ @PCN-222(Fe)-3.5 h-60 °C (10)	30	98
4	CsCu ₂ I ₃ @PCN-222(Fe)-3.5 h-r.t. (10)	~30	98
5	PCN-222(Fe) (7)	60	
6	CsCu ₂ I ₃ (7)	30	80
7	PCN-222(Fe) (7) + CsCu ₂ I ₃ (7)	30	85

^aReaction conditions: benzyl chloride (0.5 mmol), NaN₃ (1 mmol), phenylacetylene (1 mmol), water (2 mL), and catalyst. ^bPurified yield.


after 85 min (Table 1, entry 1). The reaction is stereoselective with the exclusive formation of the 1,4-isomer without any observation of the 1,5-isomer.³⁴ Water and water-miscible organic solvent mixtures have been reported as CuAAC reaction media.^{33,35–37} Organic reactions in water lacking an organic solvent offer a significant advantage from the environmental point of view, provided that substrates and reagents are soluble in this medium. Since the pore surface is predominantly lined with the hydrophobic organic linkers, the PCN framework has a preference in aqueous solution for adsorption of the organic starting materials into the cavity *via* “hydrophobic–hydrophobic interactions”,³⁷ thereby increasing the concentration of substrates near the active sites, which increases the catalytic reaction rate and selectivity. When the Cu content increased to 1.93 wt % (CsCu₂I₃@PCN-222(Fe)-15 min-60 °C, 13.66 wt % zirconium), although the BET surface area and porosity slightly decreased, the activity was almost coincident with that of CsCu₂I₃@PCN-222(Fe)-15 min-r.t. (yield of 98% at 80 min) (Table 1, entry 2). When CsCu₂I₃ was increased to 11.85 wt % copper (2.94 wt % zirconium) in the case of CsCu₂I₃@PCN-222(Fe)-3.5 h-60 °C, the product yield of 98% was achieved at a shorter reaction time of 30 min in comparison with the 15 min samples (Table 1, entry 3). The activity of CsCu₂I₃@PCN-222(Fe) with 13.88 wt % copper (CsCu₂I₃@PCN-222(Fe)-3.5 h-r.t.) was almost the same as that of CsCu₂I₃@PCN-222(Fe)-3.5 h-60 °C with similar porosity and metal content (Table 1, entry 4). The data revealed that a balance between porosity and CsCu₂I₃ loading seems to play an essential role in the performance enhancement of CsCu₂I₃@PCN-222(Fe) in this reaction. In other control tests, the catalytic activity of the constructed PCN-222(Fe) and CsCu₂I₃ was also considered for comparison (Table 1, entries 5–7). PCN-222(Fe) showed no catalytic activity and gave no product after 1 h (Table 1, entry 5). For CsCu₂I₃, the obtained yield was lower than that of the porous CsCu₂I₃@PCN-222(Fe)-3.5 h (Table 1, entry 6 *vs* entries 3 and 4). When physically mixed PCN-222(Fe) and CsCu₂I₃ were used as a catalyst, the product yield was still lower than that of CsCu₂I₃@PCN-222(Fe)-3.5 h-60 °C (Table 1, entry 7).

To show the excellent catalytic performance of our host-guest material, the activity of CsCu₂I₃@PCN-222(Fe) was compared with that of previously reported catalysts in this reaction, as given in Table S3. As can be seen in Table S3, the previously reported catalysts such as CuI@UiO-67-IM (IM = imidazolium salt),³⁶ CuSO₄·5H₂O/sodium ascorbate/ β -cyclodextrin,³⁷ Cu-tetracatechol metallopolymer,³⁸ CuI 1D polymeric coordination complex,³⁹ and self-assembled poly-(imidazole-acrylamide)-Cu/sodium ascorbate⁴⁰ generally exhibit lower catalytic activity or low selectivity and require higher temperature or longer reaction time in comparison with the use of the CsCu₂I₃@PCN-222(Fe) catalyst. Moreover, CsCu₂I₃@PCN-222(Fe) was successfully reused and maintained its outstanding performance for the click reaction in terms of both activity and selectivity (Figure S9). The superior performance of CsCu₂I₃@PCN-222(Fe) is attributed to the stabilization by confinement and isolation of the CsCu₂I₃ active sites within the MOF while still being accessible due to the porosity of the MOF host.

Tandem/cascade reactions, consisting in multistep sequential reactions performed in one pot, are exciting reactions in modern chemistry that can minimize wastes, diminish energy consumption, avoid intermediate workups, and optimize the

use of resources.⁴¹ We then were interested in investigating the activity of the synthesized CsCu₂I₃@PCN-222(Fe) composites as heterogeneous catalysts for one-pot cascade selective photo-oxidation of benzyl alcohols/*in situ* Knoevenagel condensation with malononitrile under visible LED illumination using oxygen (balloon, 1 atm.) as a green oxidant in acetonitrile (Table 2). There was nearly no product in the absence of

Table 2. Benzylidenemalononitrile Formation via One-Pot Selective Photo-oxidation/Knoevenagel Condensation Cascade Reaction under Different Conditions^a



entry	catalyst (mg)	time (h)	yield (%) ^b
1 ^c		15	
2 ^d	CsCu ₂ I ₃ @PCN-222(Fe)-3.5 h-60 °C (15)	15	trace
3	CsCu ₂ I ₃ @PCN-222(Fe)-3.5 h-60 °C (15)	15	96
4	CsCu ₂ I ₃ @PCN-222(Fe)-15 min-60 °C (15)	15	67
5 ^e	CsCu ₂ I ₃ @PCN-222(Fe)-3.5 h-60 °C (15)	15	
6	CsCu ₂ I ₃ (11)	24	34
7	PCN-222(Fe) (10)	24	60
8	PCN-222(Fe) (10) + CsCu ₂ I ₃ (11)	15	71

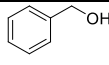
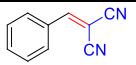
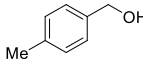
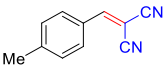
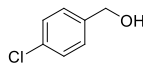
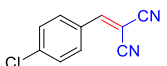
^aReaction conditions: benzyl alcohol (0.5 mmol), malononitrile (0.75 mmol), acetonitrile (2–3 mL), and catalyst. ^bPurified product. ^cIn the absence of the catalyst. ^dIn the absence of visible LED light irradiation. ^eN₂ instead O₂.

either CsCu₂I₃@PCN-222(Fe)-3.5 h-60 °C or visible light (Table 2, entries 1 and 2). In the presence of CsCu₂I₃@PCN-222(Fe)-3.5 h-60 °C, the reaction proceeded efficiently upon LED irradiation. The isolated yield of the benzylidenemalononitrile product reached 96% after 15 h with full conversion of benzyl alcohol (>99%) (Table 2, entry 3). It was also found that CsCu₂I₃-loaded PCN-222(Fe) with the lowest amount of copper (CsCu₂I₃@PCN-222(Fe)-15 min-60 °C) could also promote the reaction and afforded a product yield of 67% within 15 h (Table 2, entry 4). When N₂ was used instead of O₂, the product yield was suppressed significantly (Table 2, entry 5), showing the role of O₂ as an oxidant. In a control experiment with pure CsCu₂I₃ under identical conditions, the yield was very low even after a prolonged time period (Table 2, entry 6). In additional experiments using pristine PCN-222(Fe) MOF and its physical mixture with CsCu₂I₃, the product yields were still lower than that of CsCu₂I₃@PCN-222(Fe)-3.5 h-60 °C (Table 2, entries 7 and 8). These results indicate that the good performance of CsCu₂I₃@PCN-222(Fe) in this reaction is ascribed to the existence of the mesoporous MOF host and CsCu₂I₃ components, establishing a synergistic effect between both of them.

The scope of the CsCu₂I₃@PCN-222(Fe) photocatalyst was then surveyed for electron-donating and electron-withdrawing groups, *e.g.*, methyl and chloride, on benzyl alcohols, as shown in Table 3. Under typical conditions, the aromatic alcohols were effectively converted to their corresponding benzylidenemalononitrile products in good yields with high selectivity (>99%) (Table 3), indicating the potential utility of this photocatalyst.

Table S4 also shows the outstanding performance of CsCu₂I₃@PCN-222(Fe) compared with the other reported (photo)catalysts^{42–46} for this reaction. Several types of

Table 3. CsCu₂I₃@PCN-222(Fe)-Catalyzed Selective One-Pot Cascade Synthesis of Benzylidenemalononitriles from Benzyl Alcohols^a

Entry	Substrate	Product	Time (h)	Yield (%) ^b
1			15	96
2			15	91
3			15	93

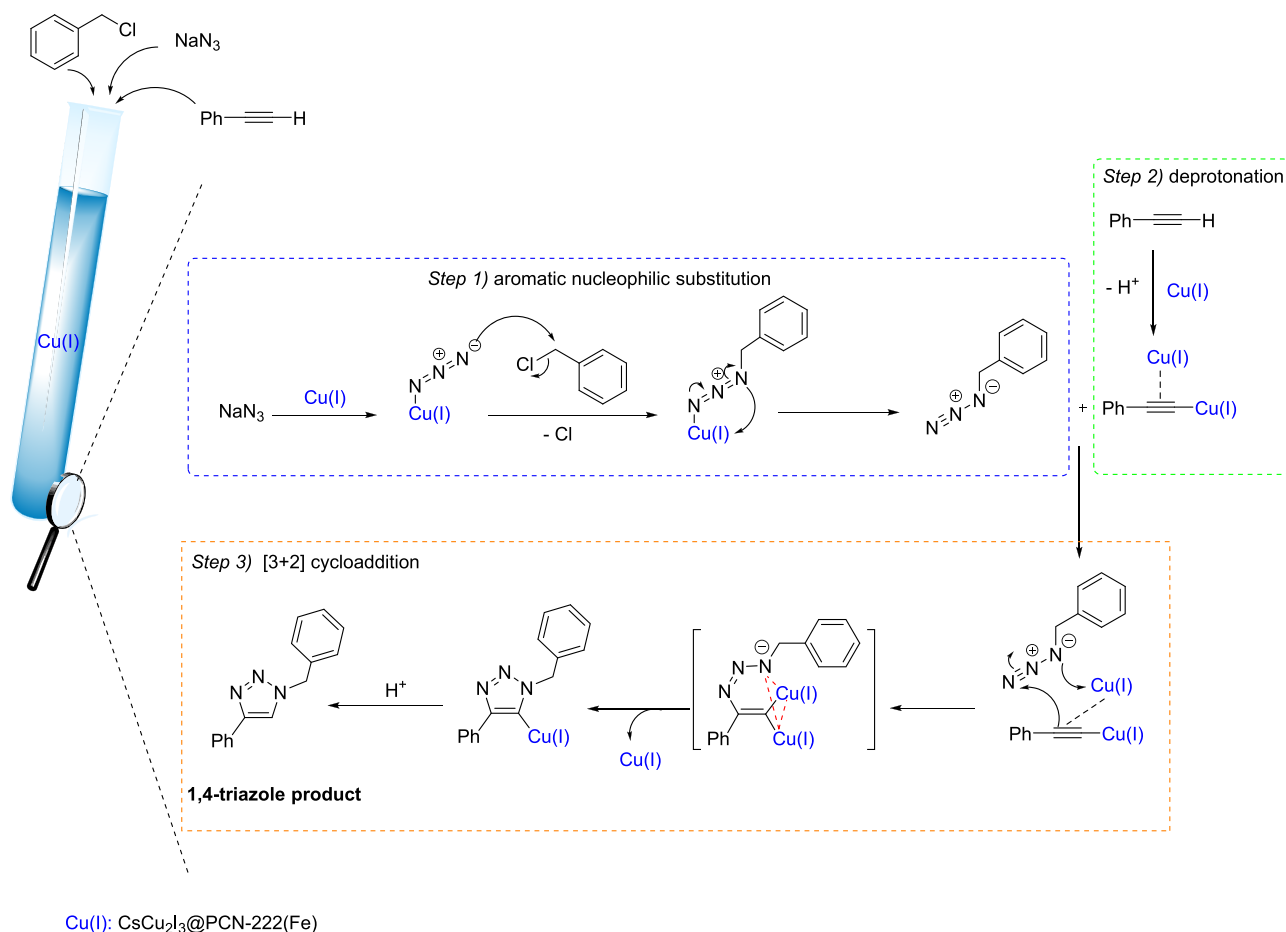
^aReaction conditions: benzyl alcohol (0.5 mmol), malononitrile (0.75 mmol), acetonitrile (2–3 mL), and catalyst (15 mg). ^bPurified products.

photocatalytic/catalytic systems including NH₂-MIL-101-(Fe),⁴³ g-C₃N₄/FeWO₄,⁴² Au(III)@Cu(II)-MOF,⁴⁴ Cu(II)/amine bifunctional MOF,⁴⁵ and Zr-MOF-NH₂⁴⁶ have been reported for the production of benzylidenemalononitrile. However, the procedures reported so far have several disadvantages including poor stability, the presence of noble metals, long reaction, the use of oxidant (*tert*-butyl hydroperoxide or hydrogen peroxide), artificial UV light, and an excess of malononitrile as well as high temperatures and high catalyst loadings, which diminish the interest of the process. On the other hand, in the recent years, due to global warming and the shift in the energy sources, conventional synthetic techniques have moved toward the use of visible light photocatalytic systems, employing LEDs that significantly reduce energy consumption.⁴⁷ Notably, the multifunctional CsCu₂I₃@PCN-222(Fe) worked well without any additive, at low catalyst loading, and with a low power light source.

Two of the main advantages of using a heterogeneous (photo)catalyst are recyclability and reusability. Therefore, the reuse experiments were performed under the best reaction conditions as presented in Figure S10. The results presented that the hybrid CsCu₂I₃@PCN-222(Fe) photocatalyst could be reused for at least four sequential reaction cycles without substantial decay in efficiency (Figure S10) after its recovery by centrifugation and washing. Atomic absorption spectroscopy (AAS) analysis of the supernatant revealed insignificant copper (0.9% of the total Cu amount in the photocatalyst) and iron leaching (0.4%). The comparison of fresh and reused PXRD profiles (Figures S11) and SEM images (Figure S12 versus Figure 2a) revealed that CsCu₂I₃@PCN-222(Fe) has retained its crystallinity and particle morphology after the cascade reaction. In addition, EDX elemental analysis of the photocatalyst indicated that the metal contents do not change significantly after its reuse (Figures S13 and S14 versus Tables S1 and S2). The recovered catalyst was further assessed by using TGA, which shows the same profile as that of the fresh one (Figure S15). All the available data indicate that CsCu₂I₃@PCN-222(Fe) is an active, stable, and reusable multifunctional catalyst. These stability data are remarkable considering the small size of the particles and the instability of iodide perovskites.

The work showed that the integration of a semiconductor-like porphyrinic MOF, PCN-222(Fe), with perovskite CsCu₂I₃

Scheme 1. Proposed Mechanism for the Click Synthesis of 1,4-Diphenyl-1,2,3-triazole by Using the CsCu₂I₃@PCN-222(Fe) Catalyst



nanocrystals results in synergistic effects derived from confinement and affords an optimized and efficient catalytic system for the tandem reaction.

3.3. Mechanistic Studies. A plausible mechanism for the three-component azide-alkyne 1,3-dipolar cycloaddition reaction toward the regioselective synthesis of 1,4-diphenyl-1,2,3-triazole is depicted in Scheme 1. CsCu₂I₃@PCN-222(Fe) including well-dispersed Cu(I) species³³ composing CsCu₂I₃ (Figures S7 and S8) can act as a heterogeneous multifunctional catalyst promoting the various sequential steps: the first step is the *in situ* generation of 1,4-phenyl azide *via* aromatic nucleophilic substitution reaction between sodium azide and benzyl bromide, the second step is the deprotonation of the terminal hydrogen of phenyl acetylene, and the third step is the [3 + 2] cycloaddition reaction between the deprotonated phenyl acetylene and the *in situ*-formed azide to afford the desired 1,4-isomer product as shown in Scheme 1. It should be noted that the mesoporous MOF host allows the accessibility of these reactants to the Cu(I) sites and prompts the reactions within the cavities.

To gain key insights into the mechanistic scenarios of the one-pot cascade transformation over CsCu₂I₃@PCN-222(Fe), additional control experiments were carried out (see Scheme S1 and also the experiments given in Table 2). In the cascade reaction between benzyl alcohol and malononitrile, benzaldehyde appears as an intermediate. Photocatalytic oxidation of benzyl alcohol to benzaldehyde takes place without over-oxidation to benzoic acid, which was barely detected during

the course of the reaction (Scheme S1a). In another control test, under the same condition, when benzyl alcohol was replaced by benzaldehyde, the desired benzylidenemalononitrile was produced quantitatively after a short reaction time of ~30 min even in the dark (Scheme S1b,c). These tests confirmed that the condensation reaction between benzaldehyde and malononitrile is easier and faster (Scheme S1) than the photo-oxidation process, which is the rate-determining step in the cascade reaction. The controls reveal that the host-guest hybrid material serves as a multifunctional (photo)-catalyst including also both Lewis acidic sites such as Fe³⁺, Zr⁴⁺, Cu⁺, and Cs⁺ (see Scheme S1 for additional experiments and Figure S16) and redox-active sites of PCN-222(Fe) and lead-free CsCu₂I₃ perovskite as the light absorber. Both components operate synergistically.

To further identify the prevalent reactive oxygen species (ROS) in the present system promoting the photo-oxidation step, inhibition experiments by adding quenchers such as 1,4-benzoquinone (superoxide radical anion (O₂^{•-}) scavenger), sodium azide (singlet oxygen (¹O₂) scavenger), and methanol (hole (h⁺) scavenger) to the reaction mixture were performed (Figure S17). The quenching study is compatible with the *in situ* formation of O₂^{•-} and ¹O₂ (main species) as well as h⁺ (minor species) during the photocatalytic process, as assessed by the decrease in product yield. Electron paramagnetic resonance (EPR) measurements were then performed to quantify the *in situ*-generated O₂^{•-} and ¹O₂ as the ROS in this system (Figure 5). Using 2,2,6,6-tetramethylpiperidine

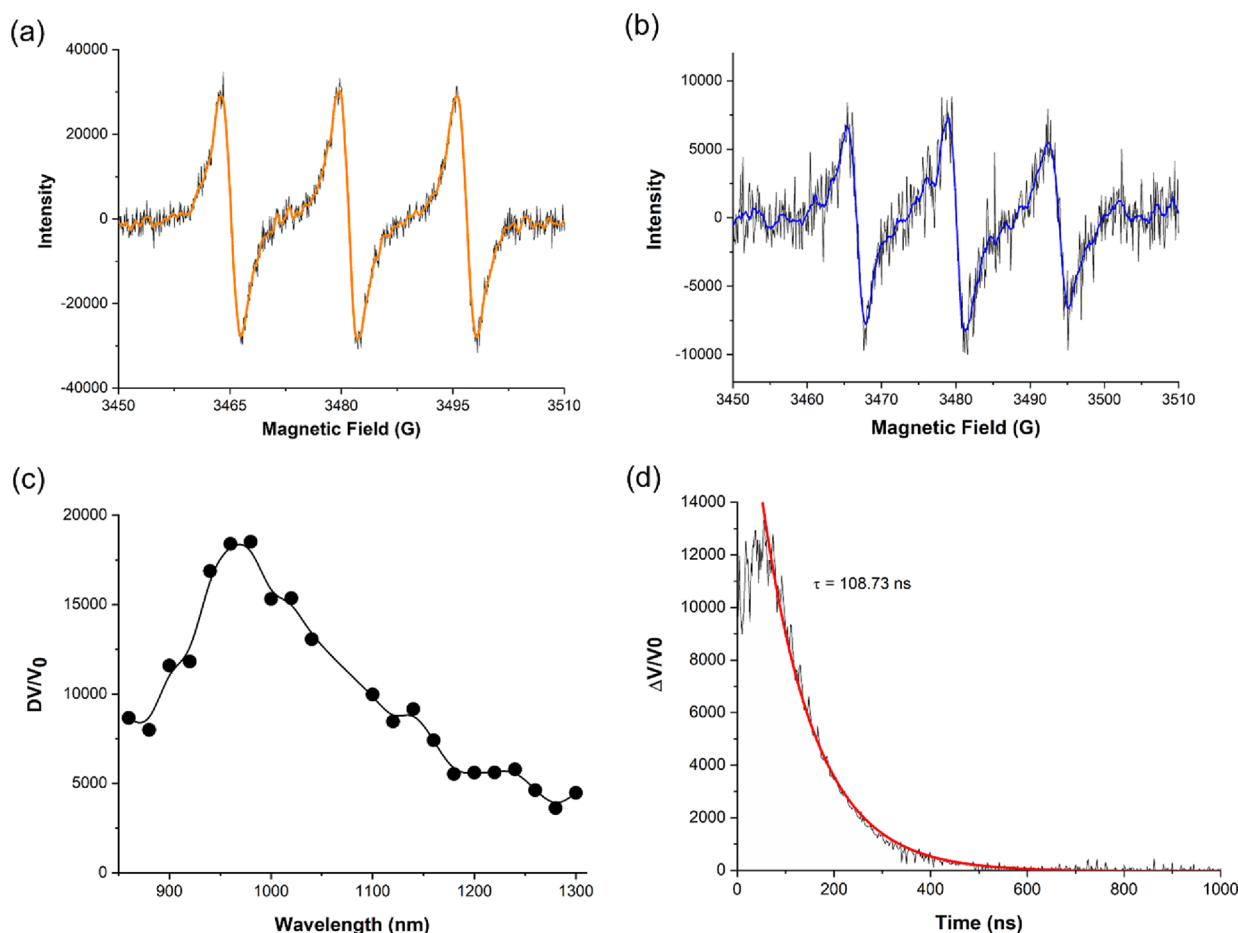


Figure 5. EPR spectra of samples of (a) TEMP or (b) DMPO with $\text{CsCu}_2\text{I}_3@\text{PCN-222}(\text{Fe})$ and O_2 under visible light irradiation, (c) time-resolved spectrum corresponding to $^1\text{O}_2$ photoluminescence, and (d) temporal signal decay profile of $^1\text{O}_2$ phosphorescence recorded for $\text{CsCu}_2\text{I}_3@\text{PCN-222}(\text{Fe})$ upon 355 nm laser excitation.

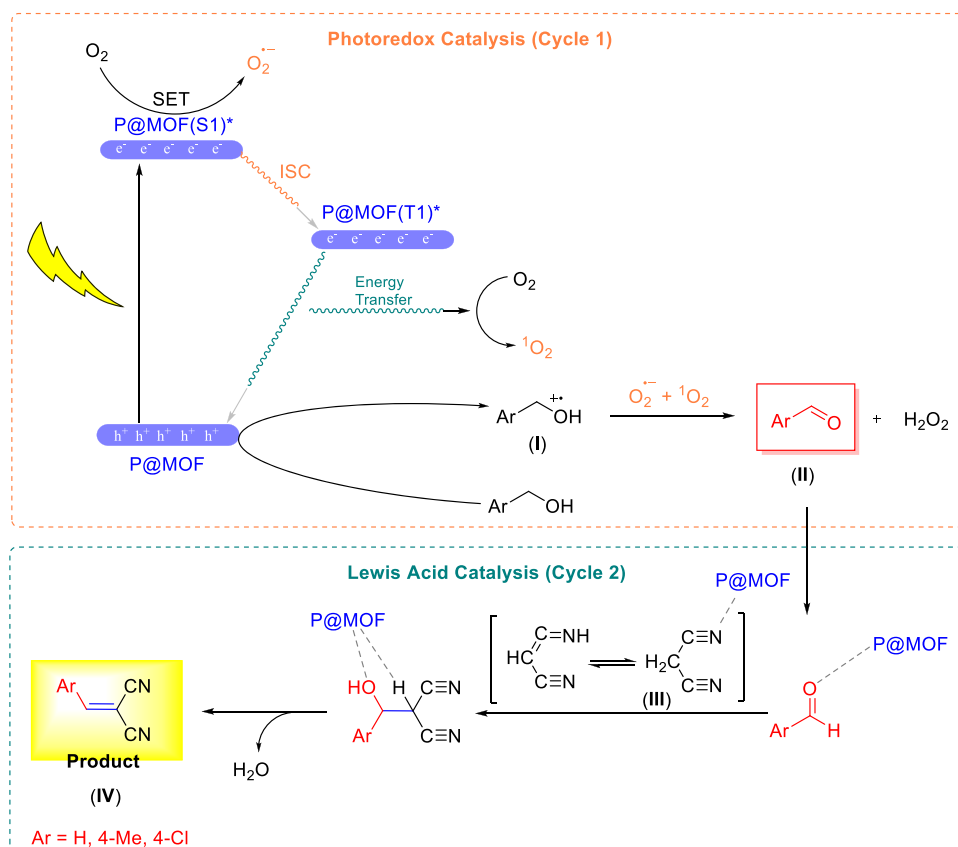
(TEMP) as a specific $^1\text{O}_2$ trapping agent, a strong triplet signal of an intensity ratio of 1:1:1, corresponding to TEMP, was detected after light irradiation, which confirmed the formation of $^1\text{O}_2$ (Figure 5a). To confirm $\text{O}_2^{\bullet-}$ generation, 5,5-dimethyl-1-pyrroline *N*-oxide (DMPO), as a specific $\text{O}_2^{\bullet-}$ trapping agent, was used, which generated multiline EPR signals after light irradiation (Figure 5b), corresponding to DMPO- $\text{O}_2^{\bullet-}$ and nitroxide-related radicals⁴⁸ resulted from $^1\text{O}_2/\text{O}_2^{\bullet-}$ -driven DMPO decomposition. It should be noted that no radical and no EPR signal were detected under dark conditions.

Furthermore, the lifetime of the singlet oxygen formed within the porous $\text{CsCu}_2\text{I}_3@\text{PCN-222}(\text{Fe})$ photocatalyst was measured by the time-resolved phosphorescence technique.⁴⁹ The method permits one to quantify directly the generation of $^1\text{O}_2$ by detecting its characteristic phosphorescence in the near-infrared (NIR) region (Figure 5c,d). Upon single-pulse laser excitation at 355 nm, the time-resolved NIR phosphorescence showed a $^1\text{O}_2$ lifetime of up to 100 ns for the $\text{CsCu}_2\text{I}_3@\text{PCN-222}(\text{Fe})$ photocatalyst.

The above-described arguments evidently confirm that $\text{CsCu}_2\text{I}_3@\text{PCN-222}(\text{Fe})$ is cooperatively capable of generating $^1\text{O}_2$, via an energy transfer pathway, and $\text{O}_2^{\bullet-}$, via a charge transfer (CT)/single electron transfer (SET) pathway, during the process while acting as an Lewis acid catalyst.

Hence, according to the control experiments, quenching and EPR tests, XPS data, time-resolved phosphorescence, and literature survey,^{22,50} a possible mechanism for the one-pot

selective photo-oxidation/Knoevenagel condensation cascade reaction can be proposed. The mechanism is depicted in Scheme 2. Upon light irradiation, the $\text{CsCu}_2\text{I}_3@\text{PCN-222}(\text{Fe})$ multifunctional catalyst (here simply denoted as P@MOF) is first excited to form the singlet excited state of the P@MOF, $[\text{P@MOF}(\text{S}_1)]^*$. $[\text{P@MOF}(\text{S}_1)]^*$ is oxidized by adsorbed O_2 to form $\text{O}_2^{\bullet-}$ over a single electron transfer (SET) process. Alternatively, $[\text{P@MOF}(\text{S}_1)]^*$ can relax vibrationally to a lower energy triplet state, $[\text{P@MOF}(\text{T}_1)]^*$, through an intersystem crossing (ISC) process and can be quenched further by O_2 to generate $^1\text{O}_2$ over an energy transfer. The generated hole (h^+) rapidly oxidizes the benzyl alcohol to generate radical cation species (I) as the intermediate, which can consequently react with the photoformed ROS ($\text{O}_2^{\bullet-}$ and $^1\text{O}_2$) to produce the corresponding aldehyde product (II) and H_2O_2 by-product. The observed selectivity of the P@MOF is likely regulated by the micro/meso-hierarchical hydrophobic structure, which allows the free diffusion of substrates/products and prevents over-oxidation by the same species of the hybrid catalyst. Next, the P@MOF including the Lewis acid sites (such as Fe^{3+} , Zr^{4+} , Cu^+ , and Cs^+) activates the *in situ*-produced aldehyde and malononitrile (III) for a nucleophilic addition of the Knoevenagel coupling reaction toward the formation of the final product (IV). Subsequently, the (photo)catalyst is ready for another round of tandem reaction.

Scheme 2. Proposed Mechanism for the Condensation Cascade Transformation over $\text{CsCu}_2\text{I}_3@\text{PCN-222}(\text{Fe})$ 

P@MOF = $\text{CsCu}_2\text{I}_3@\text{PCN-222}(\text{Fe})$

4. CONCLUSIONS

Briefly, tetrametallic multifunctional porous $\text{CsCu}_2\text{I}_3@\text{PCN-222}(\text{Fe})$ hybrid materials have been creatively planned and fabricated by post-synthetic modification of iron-porphyrin PCN-222(Fe) with the earth-abundant and lead-free CsCu_2I_3 perovskite *via* the antisolvent protocol using the MOF and the same amount of CsCu_2I_3 precursors (CuI and CsI). Characterization of $\text{CsCu}_2\text{I}_3@\text{PCN-222}(\text{Fe})$ rods shows unique structural and functional properties arising from the collective active sites of the CsCu_2I_3 nanoparticles incorporated inside the MOF pores, providing stabilization of the iodide perovskite. These properties have allowed the use of $\text{CsCu}_2\text{I}_3@\text{PCN-222}(\text{Fe})$ as a heterogeneous catalyst, revealing a remarkable catalytic activity for the three-component click reaction and one-pot selective photo-oxidation/Knoevenagel domino reaction with oxygen (1 atm) under visible light. The $\text{CsCu}_2\text{I}_3@\text{PCN-222}(\text{Fe})$ composite performs better than benchmark catalysts for these two processes. The activity appears to be a balance between porosity and CsCu_2I_3 loading. Outstandingly, $\text{CsCu}_2\text{I}_3@\text{PCN-222}(\text{Fe})$ was stable under reaction conditions and can be reused several times. Considering the diversity of halide perovskites, our results open the way to exploit the potential in the catalysis of these materials upon encapsulation inside MOFs.

■ ASSOCIATED CONTENT

SI Supporting Information

The Supporting Information is available free of charge at <https://pubs.acs.org/doi/10.1021/acsami.2c04364>.

Details of characterizations (SEM images, EDS analyses, mapping elemental analyses, N_2 adsorption–desorption measurements, pore size distributions, UV–Vis DRS spectra, Tauc plots, TGA profiles, XPS spectra, PXRD patterns, melting points, and NMR spectra), control experiments, recycling tests, inhibition investigation, and comparison tables with other materials (PDF)

■ AUTHOR INFORMATION

Corresponding Authors

Mostafa Khajeh – Department of Chemistry, University of Zabol, Zabol 98615-538, Iran; orcid.org/0000-0002-7097-2898; Phone: +98-915-142-3614; Email: m_khajeh@uoz.ac.ir

Ali Reza Oveisi – Department of Chemistry, University of Zabol, Zabol 98615-538, Iran; orcid.org/0000-0002-0075-211X; Phone: +98-915-542-8132; Email: aroveisi@uoz.ac.ir

Hermenegildo García – Departamento de Química and Instituto de Tecnología Química CSIC-UPV, Universitat Politècnica de València, 46022 Valencia, Spain; orcid.org/0000-0002-9664-493X; Phone: +34-96-387-7807; Email: hgarcia@qim.upv.es

Authors

Saba Daliran – Department of Chemistry, University of Zabol, Zabol 98615-538, Iran

Josep Albero – Departamento de Química and Instituto de Tecnología Química CSIC-UPV, Universitat Politècnica de

València, 46022 Valencia, Spain; orcid.org/0000-0002-4841-7206

Complete contact information is available at:
<https://pubs.acs.org/10.1021/acsami.2c04364>

Author Contributions

All authors reviewed the results and approved the final version of the manuscript.

Notes

The authors declare no competing financial interest.

ACKNOWLEDGMENTS

This work was supported by the Iran National Science Foundation (INSF) (project number: 98024397) and the Iran Science Elites Federation (ISEF). Also, financial support by the University of Zabol is gratefully acknowledged (grant number: IR-UOZ-GR-9381). We thank M. A. Forneli Rubio for the help with steady-state UV–Vis, photoemission, and TEM experiments.

REFERENCES

- (1) Lin, R.; Guo, Q.; Zhu, Q.; Zhu, Y.; Zheng, W.; Huang, F. All-Inorganic CsCu₂I₃ Single Crystal with High-PLQY ($\approx 15.7\%$) Intrinsic White-Light Emission via Strongly Localized 1D Excitonic Recombination. *Adv. Mater.* **2019**, *31*, 1905079.
- (2) Xiang, W.; Liu, S.; Tress, W. A Review on the Stability of Inorganic Metal Halide Perovskites: Challenges and Opportunities for Stable Solar Cells. *Energy Environ. Sci.* **2021**, *14*, 2090–2113.
- (3) Ho, K.; Wei, M.; Sargent, E. H.; Walker, G. C. Grain Transformation and Degradation Mechanism of Formamidinium and Cesium Lead Iodide Perovskite under Humidity and Light. *ACS Energy Lett.* **2021**, *6*, 934–940.
- (4) Jena, A. K.; Kulkarni, A.; Miyasaka, T. Halide Perovskite Photovoltaics: Background, Status, and Future Prospects. *Chem. Rev.* **2019**, *119*, 3036–3103.
- (5) Mo, X.; Li, T.; Huang, F.; Li, Z.; Zhou, Y.; Lin, T.; Ouyang, Y.; Tao, X.; Pan, C. Highly-Efficient All-Inorganic Lead-Free 1d CsCu₂I₃ Single Crystal for White-Light Emitting Diodes and UV Photo-detection. *Nano Energy* **2021**, *81*, No. 105570.
- (6) Vashishtha, P.; Nutan, G. V.; E. Griffith, B.; Fang, Y.; Giovanni, D.; Jagadeeswararao, M.; Sum, T. C.; Mathews, N.; Mhaisalkar, S. G.; Hanna, J. V.; White, T. Cesium Copper Iodide Tailored Nanoplates and Nanorods for Blue, Yellow, and White Emission. *Chem. Mater.* **2019**, *31*, 9003–9011.
- (7) Li, Y.; Shi, Z.; Wang, L.; Chen, Y.; Liang, W.; Wu, D.; Li, X.; Zhang, Y.; Shan, C.; Fang, X. Solution-Processed One-Dimensional CsCu₂I₃ Nanowires for Polarization-Sensitive and Flexible Ultraviolet Photodetectors. *Mater. Horizons* **2020**, *7*, 1613–1622.
- (8) Fang, S.; Wang, Y.; Li, H.; Fang, F.; Jiang, K.; Liu, Z.; Li, H.; Shi, Y. Rapid Synthesis and Mechanochemical Reactions of Cesium Copper Halides for Convenient Chromaticity Tuning and Efficient White Light Emission. *J. Mater. Chem. C* **2020**, *8*, 4895–4901.
- (9) He, M.; Cheng, Y.; Shen, L.; Shen, C.; Zhang, H.; Xiang, W.; Liang, X. Mn-Doped CsPbCl₃ Perovskite Quantum Dots (PQDs) Incorporated into Silica/Alumina Particles Used for WLEDs. *Appl. Surf. Sci.* **2018**, *448*, 400–406.
- (10) Malgras, V.; Tominaka, S.; Ryan, J. W.; Henzie, J.; Takei, T.; Ohara, K.; Yamauchi, Y. Observation of Quantum Confinement in Monodisperse Methylammonium Lead Halide Perovskite Nanocrystals Embedded in Mesoporous Silica. *J. Am. Chem. Soc.* **2016**, *138*, 13874–13881.
- (11) Zhou, Q.; Bai, Z.; Lu, W.-g.; Wang, Y.; Zou, B.; Zhong, H. In Situ Fabrication of Halide Perovskite Nanocrystal-Embedded Polymer Composite Films with Enhanced Photoluminescence for Display Backlights. *Adv. Mater.* **2016**, *28*, 9163–9168.
- (12) Yadav, S. K.; Grandhi, G. K.; Dubal, D. P.; de Mello, J. C.; Otyepka, M.; Zbořil, R.; Fischer, R. A.; Jayaramulu, K. Metal Halide Perovskite@Metal-Organic Framework Hybrids: Synthesis, Design, Properties, and Applications. *Small* **2020**, *16*, 2004891.
- (13) Qiu, L.; Xing, K.; Zhang, J.; Yang, Y.; Cao, W.; Zhou, X.; Zhu, K.; Xia, D.; Fan, R. Two-Dimensional Metal–Organic Frameworks-Based Grain Termination Strategy Enables High-Efficiency Perovskite Photovoltaics with Enhanced Moisture and Thermal Stability. *Adv. Funct. Mater.* **2021**, *31*, 2010368.
- (14) Zhang, C.; Li, W.; Li, L. Metal Halide Perovskite Nanocrystals in Metal–Organic Framework Host: Not Merely Enhanced Stability. *Angew. Chem., Int. Ed.* **2021**, *60*, 7488–7501.
- (15) He, H.; Cui, Y.; Li, B.; Wang, B.; Jin, C.; Yu, J.; Yao, L.; Yang, Y.; Chen, B.; Qian, G. Confinement of Perovskite-QDs Within a Single MOF Crystal for Significantly Enhanced Multiphoton Excited Luminescence. *Adv. Mater.* **2019**, *31*, 1806897.
- (16) Islamoglu, T.; Chen, Z.; Wasson, M. C.; Buru, C. T.; Kirlikovali, K. O.; Afrin, U.; Mian, M. R.; Farha, O. K. Metal–Organic Frameworks Against Toxic Chemicals. *Chem. Rev.* **2020**, *120*, 8130–8160.
- (17) Melillo, A.; Cabrero-Antonino, M.; Navalón, S.; Álvaro, M.; Ferrer, B.; García, H. Enhancing Visible-Light Photocatalytic Activity for Overall Water Splitting in UiO-66 by Controlling Metal Node Composition. *Appl. Catal., B* **2020**, *278*, No. 119345.
- (18) Pascanu, V.; González Miera, G.; Inge, A. K.; Martín-Matute, B. Metal–Organic Frameworks as Catalysts for Organic Synthesis: A Critical Perspective. *J. Am. Chem. Soc.* **2019**, *141*, 7223–7234.
- (19) Wang, Q.; Astruc, D. State of the Art and Prospects in Metal–Organic Framework (MOF)-Based and MOF-Derived Nanocatalysis. *Chem. Rev.* **2020**, *120*, 1438–1511.
- (20) Oudi, S.; Oveisi, A. R.; Daliran, S.; Khajeh, M.; Luque, R.; Sen, U.; García, H. Straightforward Synthesis of a Porous Chromium-Based Porphyrinic Metal-Organic Framework for Visible-Light Triggered Selective Aerobic Oxidation of Benzyl Alcohol to Benzaldehyde. *Appl. Catal., A* **2021**, *611*, No. 117965.
- (21) Daliran, S.; Ghazagh-Miri, M.; Oveisi, A. R.; Khajeh, M.; Navalón, S.; Álvaro, M.; Ghaffari-Moghaddam, M.; Samareh Delarami, H.; García, H. A Pyridyltriazol Functionalized Zirconium Metal–Organic Framework for Selective and Highly Efficient Adsorption of Palladium. *ACS Appl. Mater. Interfaces* **2020**, *12*, 25221–25232.
- (22) Zhang, X.; Wasson, M. C.; Shayan, M.; Berdichevsky, E. K.; Ricardo-Noordberg, J.; Singh, Z.; Papazyan, E. K.; Castro, A. J.; Marino, P.; Ajoyan, Z.; Chen, Z.; Islamoglu, T.; Howarth, A. J.; Liu, Y.; Majewski, M. B.; Katz, M. J.; Mondloch, J. E.; Farha, O. K. A Historical Perspective on Porphyrin-Based Metal–Organic Frameworks and Their Applications. *Coord. Chem. Rev.* **2021**, *429*, No. 213615.
- (23) Feng, D.; Gu, Z.-Y.; Li, J.-R.; Jiang, H.-L.; Wei, Z.; Zhou, H.-C. Zirconium-Metalloporphyrin PCN-222: Mesoporous Metal–Organic Frameworks with Ultrahigh Stability as Biomimetic Catalysts. *Angew. Chem., Int. Ed.* **2012**, *51*, 10307–10310.
- (24) Pratik, S. M.; Gagliardi, L.; Cramer, C. J. Engineering Electrical Conductivity in Stable Zirconium-Based PCN-222 MOFs with Permanent Mesoporosity. *Chem. Mater.* **2020**, *32*, 6137–6149.
- (25) Lu, Z.; Liu, J.; Zhang, X.; Liao, Y.; Wang, R.; Zhang, K.; Lyu, J.; Farha, O. K.; Hupp, J. T. Node-Accessible Zirconium MOFs. *J. Am. Chem. Soc.* **2020**, *142*, 21110–21121.
- (26) Drout, R. J.; Gaidimas, M. A.; Farha, O. K. Thermochemical Investigation of Oxyanion Coordination in a Zirconium-Based Metal–Organic Framework. *ACS Appl. Mater. Interfaces* **2021**, *13*, 51886–51893.
- (27) Sun, X.; Yang, J.; Wu, Z.; Meng, G.; Guo, X.; Kuang, D.; Xiong, L.; Qu, W.; Fang, X.; Yang, X.; Tang, X.; He, Y. Lead-Free CsCu₂I₃ Perovskite Nanostructured Networks Gas Sensor for Selective Detection of Trace Nitrogen Dioxide at Room Temperature. *IEEE Sens. J.* **2021**, *21*, 14677–14684.

- (28) Lu, Y.; Li, G.; Fu, S.; Fang, S.; Li, L. CsCu₂I₃ Nanocrystals: Growth and Structural Evolution for Tunable Light Emission. *ACS Omega* **2021**, *6*, 544–552.
- (29) Curran, C. D.; Lu, L.; Kiely, C. J.; McIntosh, S. Ambient Temperature Aqueous Synthesis of Ultrasmall Copper Doped Ceria Nanocrystals for the Water Gas Shift and Carbon Monoxide Oxidation Reactions. *J. Mater. Chem. A* **2018**, *6*, 244–255.
- (30) Engelhardt, L. M.; Healy, P. C.; Shephard, R. M.; Skelton, B. W.; White, A. H. Lewis-Base Adducts of Group 11 Metal(I) Compounds. 47. A Novel Series of 1:1, 2:1, and 3:1 Heterobimetallic Adducts from the Reaction of Copper(I) Halides with Tris-(dithiocarbamate)cobalt(III) Complexes. *Inorg. Chem.* **1988**, *27*, 2371–2373.
- (31) Deroubaix, G.; Marcus, P. X-Ray Photoelectron Spectroscopy Analysis of Copper and Zinc Oxides and Sulphides. *Surf. Interface Anal.* **1992**, *18*, 39–46.
- (32) Kolb, H. C.; Finn, M. G.; Sharpless, K. B. Click chemistry: diverse chemical function from a few good reactions. *Angew. Chem. Int. Ed.* **2001**, *40*, 2004–2021.
- (33) Devaraj, N. K.; Finn, M. G. Introduction: Click Chemistry. *Chem. Rev.* **2021**, *121*, 6697–6698.
- (34) Creary, X.; Anderson, A.; Brophy, C.; Crowell, F.; Funk, Z. Method for Assigning Structure of 1,2,3-Triazoles. *J. Org. Chem.* **2012**, *77*, 8756–8761.
- (35) Mathew, P.; Sasidharan, D.; Rakesh, N. P. Copper(I) Stabilized on *N,N'*-Methylene Bis-Acrylamide Crosslinked Polyvinylpyrrolidone: An Efficient Reusable Catalyst for Click Synthesis of 1,2,3-Triazoles in Water. *Appl. Organomet. Chem.* **2020**, *34*, No. e5642.
- (36) Hu, Y.-H.; Wang, J.-C.; Yang, S.; Li, Y.-A.; Dong, Y.-B. Cui@UiO-67-Im: A MOF-Based Bifunctional Composite Triphase-Transfer Catalyst for Sequential One-Pot Azide–Alkyne Cycloaddition in Water. *Inorg. Chem.* **2017**, *56*, 8341–8347.
- (37) Shin, J.-A.; Lim, Y.-G.; Lee, K.-H. Copper-Catalyzed Azide–Alkyne Cycloaddition Reaction in Water Using Cyclodextrin as a Phase Transfer Catalyst. *J. Org. Chem.* **2012**, *77*, 4117–4122.
- (38) Joshi, S.; Yip, Y. J.; Türel, T.; Verma, S.; Valiyaveetil, S. Cu–Tetracatechol Metallopolymer Catalyst for Three Component Click Reactions and β -Borylation of α,β -Unsaturated Carbonyl Compounds. *Chem. Commun.* **2020**, *56*, 13044–13047.
- (39) Saha, S.; Biswas, K.; Basu, B. 1-D Copper(I) Coordination Polymer Based on Bidentate 1,3-Dithioether Ligand: Novel Catalyst for Azide–Alkyne–Cycloaddition (AAC) Reaction. *Tetrahedron Lett.* **2018**, *59*, 2541–2545.
- (40) Yamada, Y. M. A.; Sarkar, S. M.; Uozumi, Y. Amphiphilic Self-Assembled Polymeric Copper Catalyst to Parts Per Million Levels: Click Chemistry. *J. Am. Chem. Soc.* **2012**, *134*, 9285–9290.
- (41) Yin, Z.; Wan, S.; Yang, J.; Kurmoo, M.; Zeng, M.-H. Recent Advances in Post-Synthetic Modification of Metal–Organic Frameworks: New Types and Tandem Reactions. *Coord. Chem. Rev.* **2019**, *378*, 500–512.
- (42) Rashidzadeh, A.; Esmaili Zand, H. R.; Ghafari, H.; Rezazadeh, Z. Graphitic Carbon Nitride Nanosheet/FeWO₄ Nanoparticle Composite for Tandem Photooxidation/Knoevenagel Condensation. *ACS Appl. Nano Mater.* **2020**, *3*, 7057–7065.
- (43) Wang, D.; Li, Z. Bi-Functional NH₂-MIL-101(Fe) for One-Pot Tandem Photo-Oxidation/Knoevenagel Condensation between Aromatic Alcohols and Active Methylene Compounds. *Catal. Sci. Technol.* **2015**, *5*, 1623–1628.
- (44) Wang, J.-S.; Jin, F.-Z.; Ma, H.-C.; Li, X.-B.; Liu, M.-Y.; Kan, J.-L.; Chen, G.-J.; Dong, Y.-B. Au@Cu(II)-MOF: Highly Efficient Bifunctional Heterogeneous Catalyst for Successive Oxidation–Condensation Reactions. *Inorg. Chem.* **2016**, *55*, 6685–6691.
- (45) Miao, Z.; Luan, Y.; Qi, C.; Ramella, D. The Synthesis of a Bifunctional Copper Metal Organic Framework and Its Application in the Aerobic Oxidation/Knoevenagel Condensation Sequential Reaction. *Dalton Trans.* **2016**, *45*, 13917–13924.
- (46) Toyao, T.; Saito, M.; Horiuchi, Y.; Matsuoka, M. Development of a Novel One-Pot Reaction System Utilizing a Bifunctional Zr-

- Based Metal–Organic Framework. *Catal. Sci. Technol.* **2014**, *4*, 625–628.
- (47) König, B. Photocatalysis in Organic Synthesis – Past, Present, and Future. *Eur. J. Org. Chem.* **2017**, *2017*, 1979–1981.
- (48) Diaz-Urbe, C. E.; Daza, M. C.; Martínez, F.; Páez-Mozo, E. A.; Guedes, C. L. B.; Di Mauro, E. Visible Light Superoxide Radical Anion Generation by Tetra(4-carboxyphenyl)porphyrin/TiO₂: EPR Characterization. *J. Photochem. Photobiol., A* **2010**, *215*, 172–178.
- (49) Cojocaru, B.; Laferrière, M.; Carbonell, E.; Parvulescu, V.; García, H.; Scaiano, J. C. Direct Time-Resolved Detection of Singlet Oxygen in Zeolite-Based Photocatalysts. *Langmuir* **2008**, *24*, 4478–4481.
- (50) Dhakshinamoorthy, A.; Li, Z.; Garcia, H. Catalysis and Photocatalysis by Metal Organic Frameworks. *Chem. Soc. Rev.* **2018**, *47*, 8134–8172.

Recommended by ACS

Recent Research Progress and Perspectives on Porphyrin-Based Porous Photocatalysts in the Field of CO₂ Reduction

Liuqing Yang, Zhaolin Li, *et al.*

AUGUST 04, 2022
ENERGY & FUELS

READ 

Selective CO₂-to-Formate Conversion Driven by Visible Light over a Precious-Metal-Free Nonporous Coordination Polymer

Yoshinobu Kamakura, Kazuhiko Maeda, *et al.*

AUGUST 05, 2022
ACS CATALYSIS

READ 

Integrating TEMPO into a Metal–Organic Framework for Cooperative Photocatalysis: Selective Aerobic Oxidation of Sulfides

Wenlong Sheng, Xianjun Lang, *et al.*

AUGUST 26, 2022
ACS CATALYSIS

READ 

Frustrated Lewis Pair Sites Boosting CO₂ Photoreduction on Cs₂CuBr₄ Perovskite Quantum Dots

Jianping Sheng, Fan Dong, *et al.*

FEBRUARY 16, 2022
ACS CATALYSIS

READ 

Get More Suggestions >